

Xumin GUO, Jin ZENG, Hui MA, Chenguang ZHAO, Lin QU, Bangchun WEN

Dynamic characteristics of a shrouded blade with impact and friction

© Higher Education Press 2020

Abstract A simplified computational model of a twisted shrouded blade with impact and friction is established. In this model, the shrouded blade is simulated by a flexible Timoshenko beam with a tip-mass, and the effects of centrifugal stiffening, spin softening, and Coriolis force are considered. Impact force is simulated using a linear spring model, and friction force is generated by a tangential spring model under sticking state and a Coulomb friction model under sliding state. The proposed model is validated by a finite element model. Then, the effects of initial gap and normal preload, coefficient of friction, and contact stiffness ratio (the ratio of tangential contact stiffness to normal contact stiffness) on system vibration responses are analyzed. Results show that resonant peaks become inconspicuous and impact plays a dominant role when initial gaps are large between adjacent shrouds. By contrast, in small initial gaps or initial normal preloads condition, resonant speed increases sharply, and the optimal initial normal preloads that can minimize resonant amplitude becomes apparent. Coefficient of friction affects the optimal initial normal preload, but it does not affect vibration responses when the contact between shrouds is under full stick. System resonant amplitude decreases with the increase of contact stiffness ratio, but the optimal initial normal preload is unaffected.

Keywords twisted shrouded blade, dynamic analysis, impact, friction, separate–stick–slip motion

Received April 12, 2019; accepted August 25, 2019

Xumin GUO, Jin ZENG, Hui MA (✉), Chenguang ZHAO, Lin QU, Bangchun WEN
School of Mechanical Engineering and Automation, Northeastern University, Shenyang 110819, China
E-mails: mahui_2007@163.com; huima@me.neu.edu.cn

Hui MA
Key Laboratory of Vibration and Control of Aero-Propulsion System
Ministry of Education, Northeastern University, Shenyang 110819, China

1 Introduction

Turbine blades of aero-engines become easily affected by high-cycle fatigue due to extreme work environments, such as high temperature, high pressure, and high rotational speed. Moreover, resonance can occur when the excitation frequency is close to the natural frequencies of blades, and large resonant amplitudes can cause high dynamic stress. High-cycle fatigue should be avoided, and the vibration amplitude of the forced blade should be reduced; thus, in high-pressure turbines of aero-engines, shrouded blades (Fig. 1) are mostly adopted to utilize the dry friction between shrouds and subsequently reduce vibration [1–3]. Many passive damping devices, such as blade–disk interfaces [4,5], under-platform dampers [6–10], and shrouds located at blade tips [11,12], have been designed to decrease vibration stress.

Many researchers have investigated the dynamic characteristics of rotating blades [13–18] and rotor structures [19–24]. Cao et al. [13] built a pre-twisted blade model with thermal barrier coating, and the effects of the working condition and the pre-twisted angle were analyzed. Wang et al. [14] used the multiple scale method to study the vibration of a turbine blade excited by air flows. With the aim of achieving a rotating tapered cantilever Timoshenko beam, Yang et al. [15,16] established a mathematical model of a beam blade with preset and pre-twist angles by using the power series method. Zeng et al. [17] introduced the crack propagation path into the vibration analysis of a rotating blade, and the influences of angular acceleration, aerodynamic force amplitude, and crack parameters on the dynamic characteristics of a cracked compressor blade are discussed. A finite element (FE) beam model with flapwise–chordwise–axial–torsional coupling was also established [18].

In many of the studies, lumped-mass models of blades with dry friction were developed to investigate the vibration reduction mechanism of the blades [25–31]. Dry friction was often modeled as massless springs and contact points by using Coulomb’s friction law, and the

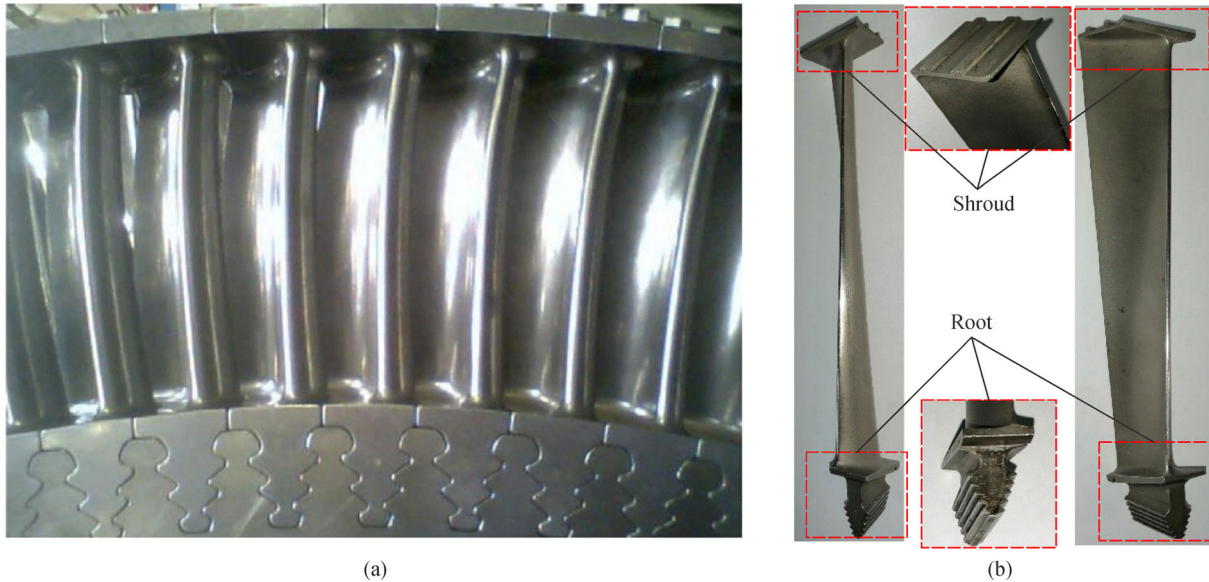


Fig. 1 Shrouded blade structures. (a) Shrouded blade group reprinted with permission from Ref. [1] from Elsevier; (b) shrouded blade.

harmonic balance method (HBM) and the direct time integration method were adopted to evaluate nonlinear dynamic responses. Wang and Shieh [27] established a 1-degree-of-freedom (1-DOF) model with dry friction by taking into consideration the influence of the variable coefficient of friction. Their simulation results were validated by experimental results obtained from the literature. On the basis of a previous work [27], a multi-HBM for solving nonlinear vibration responses was proposed to improve on calculation efficiency [28], and the proposed method was verified by the direct time integration method. With the aim of improving the computational efficiency of the traditional method, which is commonly used to solve dry friction-damped blade problems, Sanliturk et al. [29] focused on the frequency domain and proposed a calculation approach for nonlinear dynamic responses. The dry friction damper in their study was considered to be equivalent to a complex stiffness model based on first-order HBM, and their simulated results were verified by an experiment.

Subsequent research focused on the effects of variable normal load on the vibration characteristics of a damped system [22,32–34]. Koh and Griffin [35] proposed an analytical approach to solve the forced response of a blade with dry friction damper, in which contact stiffness was defined by elasticity mechanics and contact theory. The simulation results obtained from the developed method were in good agreement with the experimental results. On the basis of the optimal approximation method, Zhang et al. [36] proposed a highly accurate and efficient numerical method that can calculate the nonlinear dynamic responses of a dry friction-damped system with local friction contact. Allara [2] developed a model by using Coulomb's friction law to characterize the friction contact

of non-spherical contact geometries under the constant coefficient of friction and an initial normal preload, and the effects of contact geometrical parameters on hysteresis loops and dissipated energy were studied. Zhao et al. [37] established a fractal friction model by employing fractal geometry and nonlinear vibration theory to describe dry friction. On the basis of the model, the nonlinear dynamic responses of a turbine blade with snubber and shroud were analyzed. Jiang et al. [38] compared the effects of axial clearance on the vibration responses of shrouded and unshrouded blades. Their results showed that the displacement of the shrouded blade was smaller than that of the unshrouded blade due to the limitation of shrouding.

The macroslip friction model was frequently adopted in many previous researches, and many researchers also have used the microslip friction model to investigate the vibration characteristics of blades with contact friction [39–43]. Marquina et al. [40] developed two friction models that considered the macroslip and the microslip, and the experimental results were compared. The differences between the two models were also discussed. Yuan et al. [42] established a 2-DOF lumped-mass model by using the microslip friction model to investigate the vibration characteristics of a damping blade. The structures of the lacing and the shroud were also simulated to study the effects of damper position on the forced responses of the blade, respectively. The same microslip friction model was applied by Giridhar et al. [43] to study the dynamic responses of a damped blade, and their simulation results were verified by a bench test. In validating theoretical results, some researchers have adopted experimental methods to investigate the dynamic characteristics of a blade system with dry friction damper [44–46].

From the above literature review, lumped-mass models

have been frequently adopted to investigate the dynamic responses of blades with friction, but these models cannot easily consider the geometrical characteristics of shrouded blades, such as their stagger angles and twist angles. Some researchers [47–50] have demonstrated that the stagger angle and the twist angle can remarkably influence the dynamic characteristics of turbine blades. The effects of the friction and the impact of the shrouded blade have been analyzed using the lumped-parameter model [34]. However, the lumped-parameter model is simplistic, and it cannot consider the influence of blade shape. Many researchers [37,40] have carried out similar studies to improve on calculation accuracy, but the focus is on the solid FE model, which may cause low computational efficiency. In overcoming this gap, the present study establishes a computational model for shrouded blades by considering the coupling effects of impact and friction. The shrouded blade is modeled using a Timoshenko beam with a stagger angle and a twist angle. The main research highlights of this study are as follows:

1) A highly efficient shrouded blade modeling method based on Ref. [50] is proposed, in which the Galerkin truncation and free-interface modal synthesis methods are used to improve on computational efficiency.

2) The influence of blade shape parameters (stagger angle and twist angle) and the coupling of impact and friction are simultaneously considered. The laws of impact and friction on the vibration reduction characteristics of the system are analyzed.

3) The proposed model is verified by two FE models with beam and shell elements.

2 Computational model and model verification

2.1 Computational model of twisted blade with impact and friction

A dynamical model of a twisted shrouded blade is established, and the impact–friction coupling effect of adjacent shrouded blades is considered (Fig. 2). In Fig. 2, $o_s v_s w_s$ denotes the shroud contact coordinate, where axis w_s is parallel to the side edge of the shroud; $o_L v_L w_L$ denotes the local coordinate on the blade tip at which the intersection angle between axis w_s and axis w_L is the shroud inclination angle α ; and $oxyz$ denotes the blade local coordinate. k_n and k_t denote normal and tangential contact stiffness on shroud contact interfaces, respectively. N_0 denotes the initial normal preload between shrouds. F_{f1} symbolizes the tangential friction force between the active blade and passive blade 1, and F_{f2} denotes the tangential friction force between the active blade and passive blade 2. Δ denotes the initial gap between the active shroud and the passive shrouds. z_{s1} denotes the tangential displacement of

the active blade shroud, and z_{s2} denotes the displacement of the contact point. μ denotes the coefficient of friction between contact interfaces.

The computational model of the shrouded blade was established in a previous work [50] by considering the effects of rotational speed and the stagger and twist angles of the blades. The equations of motion of the shrouded blade can be expressed as

$$M\ddot{q} + (G + D)\dot{q} + (K_e + K_c + K_s + K_{acc})q = F, \quad (1)$$

where M , G , D , K_e , K_c , K_s , K_{acc} , q , and F are mass matrix, Coriolis force matrix, damping matrix, structural stiffness matrix, centrifugal stiffening matrix, spin softening matrix, stiffness matrix caused by angular acceleration, canonical coordinates vector, and canonical external force vector, respectively. In this study, Rayleigh damping is adopted, and its expression is given by

$$D = \alpha M + \beta K, \quad (2)$$

where $\alpha = \frac{4\pi f_{n1} f_{n2} (f_{n1} \xi_2 - f_{n2} \xi_1)}{(f_{n1}^2 - f_{n2}^2)}$, $\beta = \frac{f_{n2} \xi_2 - f_{n1} \xi_1}{\pi(f_{n1}^2 - f_{n2}^2)}$, f_{n1} and f_{n2} represent the first two-order natural frequencies, and ξ_1 and ξ_2 are the first two-order modal damping ratios corresponding to natural frequencies with value set to $\xi_1 = 0.02$ and $\xi_2 = 0.04$. Other expressions of the matrices and details of the modeling process can be found in Ref. [50].

During shrouded blade modeling, the torsional vibration of the blade is restrained. Five shape functions are used in this study. The first four natural frequencies under different modal truncations at $\Omega = 8500$ r/min are listed in Table 1. The number of modal truncations is checked from $N = 4$ to $N = 7$ by comparing the first four modes. The convergence analysis shows that $N = 6$ is appropriate, and the maximum error is approximately 0.64% (Table 1). As such, the dimensions of mass, stiffness, and damping matrices are all 30×30 .

The normal impact force (N_1 , N_2) and the tangential friction force (F_{f1} , F_{f2}) of the contact interfaces between adjacent shrouds will change in different contact states (separate, stick, or slip). Furthermore, the normal loads between adjacent shroud contact interfaces are given as follows:

$$N_1 = \begin{cases} 0 & N_0 - k_n v_s \leq 0 \text{ Separate,} \\ N_0 - k_n v_s & \text{Contact,} \end{cases} \quad (3)$$

$$N_2 = \begin{cases} 0 & N_0 + k_n v_s \leq 0 \text{ Separate,} \\ N_0 + k_n v_s & \text{Contact,} \end{cases}$$

where v_s is the displacement of the active blade in the normal direction of the shroud.

In Eq. (3), a negative N_0 indicates the existence of an initial gap in the contact interfaces ($\Delta = -N_0/k_n$, $k_n = 1 \times 10^7$ N/m in this study). Adjacent shrouded blades are

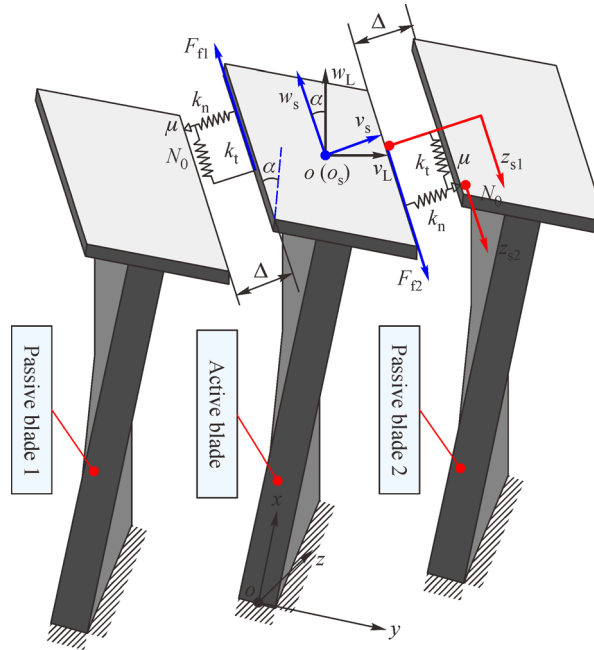


Fig. 2 Schematic of twisted shrouded blade with impact and friction.

Table 1 First four natural frequencies under different modal truncations at $\Omega = 8500$ r/min

N	f_{n1}/Hz	f_{n2}/Hz	f_{n3}/Hz	f_{n4}/Hz	Error for $f_{n1}/\%$	Error for $f_{n2}/\%$	Error for $f_{n3}/\%$	Error for $f_{n4}/\%$
4	286.0 (282.4)	1121.2 (1117.0)	1506.7 (1497.5)	3975.1 (3958.1)	1.27	0.38	0.61	0.43
5	285.3 (282.4)	1120.9 (1117.0)	1502.9 (1497.5)	3972.6 (3958.1)	1.03	0.35	0.36	0.37
6	284.2 (282.4)	1119.9 (1117.0)	1502.0 (1497.5)	3968.3 (3958.1)	0.64	0.26	0.30	0.26
7	283.6 (282.4)	1119.9 (1117.0)	1500.8 (1497.5)	3969.7 (3958.1)	0.42	0.26	0.22	0.29

Note: Values in () denotes the results obtained from FE model.

separate when $N_i = 0$ ($i = 1, 2$), and they are in contact when $N_i > 0$ ($i = 1, 2$). The tangential friction force F_{f1} between the active blade and passive blade 1 and the tangential friction force F_{f2} between the active blade and passive blade 2 are as follows:

$$F_{f1} = \begin{cases} 0 & N_1 = 0 & \text{Separate,} \\ k_t(z_{s1} - z_{s2}) & |z_{s1} - z_{s2}| \leq \mu N_1/k_t & \text{Stick,} \\ \mu N_1 \text{sign}(\dot{z}_{s2}) & |z_{s1} - z_{s2}| > \mu N_1/k_t & \text{Slip,} \end{cases}$$

$$F_{f2} = \begin{cases} 0 & N_2 = 0 & \text{Separate,} \\ k_t(z_{s1} - z_{s3}) & |z_{s1} - z_{s3}| \leq \mu N_2/k_t & \text{Stick,} \\ \mu N_2 \text{sign}(\dot{z}_{s3}) & |z_{s1} - z_{s3}| > \mu N_2/k_t & \text{Slip,} \end{cases} \quad (4)$$

where z_{s1} is the tangential displacement of the active blade shroud, and z_{s2} and z_{s3} denote the displacements of the contact points. The superposed dot denotes the time derivative.

The motion states of the contact points can be

determined by the following expressions:

$$z_{s2}(t) = \begin{cases} z_{s1}(t) & N_1 = 0 & \text{Separate,} \\ z_{s2}(t - \Delta t) & |z_{s1} - z_{s2}| \leq \mu N_1/k_t & \text{Stick,} \\ z_{s2}(t) - \mu N_1 \text{sign}(\dot{z}_{s2}(t))/k_t & |z_{s1} - z_{s2}| > \mu N_1/k_t & \text{Slip,} \end{cases}$$

$$z_{s3}(t) = \begin{cases} \dot{z}_{s1}(t) & N_1 = 0 & \text{Separate,} \\ 0 & |z_{s1} - z_{s2}| \leq \mu N_1/k_t & \text{Stick,} \\ \dot{z}_{s1}(t) & |z_{s1} - z_{s2}| > \mu N_1/k_t & \text{Slip,} \end{cases} \quad (5)$$

$$z_{s3}(t) = \begin{cases} z_{s1}(t) & N_2 = 0 & \text{Separate,} \\ z_{s3}(t - \Delta t) & |z_{s1} - z_{s3}| \leq \mu N_2/k_t & \text{Stick,} \\ z_{s3}(t) - \mu N_2 \text{sign}(\dot{z}_{s3}(t))/k_t & |z_{s1} - z_{s3}| > \mu N_2/k_t & \text{Slip,} \end{cases}$$

$$\dot{z}_{s3}(t) = \begin{cases} \dot{z}_{s1}(t) & N_2 = 0 & \text{Separate,} \\ 0 & |z_{s1} - z_{s3}| \leq \mu N_2 / k_t & \text{Stick,} \\ \dot{z}_{s1}(t) & |z_{s1} - z_{s3}| > \mu N_2 / k_t & \text{Slip.} \end{cases} \quad (6)$$

A coordinate transformation is used to transform the displacement of the blade tip under the blade local coordinate system ($ov_L w_L$) into the normal and tangential displacement of the shroud under the shroud contact coordinate ($os_v s w_s$), and the transformation equations is given by

$$\begin{bmatrix} v_s \\ w_s \end{bmatrix} = \begin{bmatrix} \cos\alpha & \sin\alpha \\ -\sin\alpha & \cos\alpha \end{bmatrix} \begin{bmatrix} v_L \\ w_L \end{bmatrix}. \quad (7)$$

Similarly, the equations used to transform the forces in the shroud contact coordinate system into those in the blade local coordinate system are written as follows:

$$\begin{bmatrix} F_y \\ F_z \end{bmatrix} = \begin{bmatrix} \cos\alpha & -\sin\alpha \\ \sin\alpha & \cos\alpha \end{bmatrix} \begin{bmatrix} N_1 - N_2 \\ F_{f1} + F_{f2} \end{bmatrix}. \quad (8)$$

By taking impact and friction into consideration, the canonical external force vector F in Eq. (1) should be replaced by \bar{F} . Therefore, the equations of motion and the expression of \bar{F} are given by

$$M\ddot{q} + (G + D)\dot{q} + (K_e + K_c + K_s + K_{acc})q = \bar{F}, \quad (9)$$

$$\bar{F} = \begin{bmatrix} F_1 \\ \bar{F}_2 \\ \bar{F}_3 \\ F_4 \\ F_5 \end{bmatrix}, \quad (10)$$

where

$$F_1(j,1) = \rho A \dot{\theta}^2 \int_0^L (R_d + x) \phi_{1j}(x) dx + m_s (R_d + L) \dot{\theta}^2 \phi_{1j}(L),$$

$$\begin{aligned} \bar{F}_2(j,1) &= -\rho A \ddot{\theta} \int_0^L \cos\beta(x) (R_d + x) \phi_{2j}(x) dx \\ &\quad - m_s (R_d + L) \ddot{\theta} \cos\beta(L) \phi_{2j}(L) \\ &\quad + \int_0^L F_e \phi_{2j}(x) dx + F_y \phi_{2j}(L), \end{aligned}$$

$$\begin{aligned} \bar{F}_3(j,1) &= \rho A \ddot{\theta} \int_0^L \sin\beta(x) (R_d + x) \phi_{2j}(x) dx \\ &\quad + m_s (R_d + L) \ddot{\theta} \sin\beta(L) \phi_{2j}(L) + F_z \phi_{2j}(L), \end{aligned}$$

$$F_4(j,1) = -\rho I_z \ddot{\theta} \int_0^L \cos\beta(x) \phi_{3j}(x) dx,$$

$$F_5(j,1) = -\rho I_y \ddot{\theta} \int_0^L \sin\beta(x) \phi_{3j}(x) dx, \quad j = 1, 2, \dots, N.$$

F_e is the uniformly distributed aerodynamic force, and its expression can be written as [3]:

$$F_e = F_0 \sin(k_e \omega t), \quad (11)$$

where $F_0 = 150$ N/m and k_e is the number of obstacles in the front of the blade ($k_e = 2$ in this study). Moreover, $\omega = 2\pi\Omega/60$, in which Ω is the rotational speed of the disk (r/min). The Newmark- β numerical method is employed to calculate vibration responses where the integration parameters are taken as: $\bar{\alpha} = 0.5$ and $\bar{\beta} = 0.25$. During the calculation process at each speed, the initial displacement, velocity and acceleration are set as zero.

A free-interface modal synthesis method is used to decrease the dimension of the computational model as means to improve on solution efficiency [51,52]. The detailed reduction process is as follows:

(1) Solve the eigenvalue λ_i and the eigenvector ξ_i of MK ($i = 1, 2, \dots, 30$).

(2) Adopt the first n -order natural frequencies of the blade, and rank the eigenvalue λ_i from smallest to largest. The dimension reduction matrix $N^* = [\xi_1, \xi_2, \dots, \xi_i, \dots, \xi_{nr}]$ can then be obtained. The eigenvector ξ_i in N^* corresponds to the eigenvalue λ_i . The dimension of N^* is $30 \times nr$.

(3) Assume $q = N^* q^*$ and the dimension of q^* to be $nr \times 1$. Substitute $q = N^* q^*$ with Eq. (9) and multiply by N^{*T} at both sides of equation. The equations of motion of the shrouded blade can then be expressed as

$$\begin{aligned} (N^{*T} M N^*) \ddot{q}^* + (N^{*T} G N^* + N^{*T} D N^*) \dot{q}^* \\ + (N^{*T} K N^*) q^* = N^{*T} F^*. \end{aligned} \quad (12)$$

After dimension reduction, with the definitions $M^* = N^{*T} M N^*$, $G^* = N^{*T} G N^*$, $D^* = N^{*T} D N^*$, and $K^* = N^{*T} K N^*$, the dimensions of mass matrix M^* , Coriolis force matrix G^* , Rayleigh damping matrix D^* , and stiffness matrix K^* become $nr \times nr$.

2.2 Model verification

2.2.1 Verification of the reduced model

The system vibration responses are compared with those obtained from the full model without reduction to verify the proposed model. The system parameters are as follows: $k_t = 1 \times 10^7$ N/m, $k_n = 1 \times 10^7$ N/m, $\alpha = 15^\circ$, and $\mu = 0.3$, and the other shrouded blade parameters are shown in Table 2. The calculations are performed using a personal computer with Intel core i7-6700 3.40 GHz processor and 16 GB RAM. After the model reduction, the convergence

results of the dimension of matrix nr with the response of the blade are determined (Fig. 1). The max error between $nr = 6$ and $nr = 30$ is approximately 0.08% (Fig. 3(b)), which shows that the reduced computational model has high accuracy. In consideration of both computational efficiency and accuracy from the analysis, $nr = 6$; thus, the dimension of the matrix can be reduced from 30×30 to 6×6 .

Different initial gaps Δ and normal preloads N_0 are considered, and the amplitude–frequency responses of the bending displacement v_L of the blade tip obtained from two models are determined (Fig. 4). The two models are in good agreement in terms of amplitude–frequency responses. In addition, the calculation time by using the reduced model is only approximately 70% of that of the full model.

2.2.2 Model verification based on the FE models

The proposed computational model is verified by comparing its results with those obtained from the two FE models by using ANSYS. The schematic of the FE model is shown in Fig. 5. In Fig. 5, $OXYZ$ and $oxyz$ denote the global coordinate system and the blade local coordinate, respectively. u , v , and w represent the displacement of an arbitrary Point P on the blade in radial, flexural, and swing directions, and u_L , v_L , and w_L denote the displacement of tip-mass Point Q in the radial, flexural, and swing directions, respectively. β_1 and β_L denote the stagger angle at the root and the blade tip of the blade, respectively.

$u_L y_s z_s$ denotes a coordinate system to describe the shroud inclination angle α , where the z_s and y_s axes are parallel and vertical to the side edge of the shroud, respectively. β_n is the angle of an arbitrary cross section between z axis and z_n axis ($\beta_n = \beta_1 + \beta'x/L$ and $\beta' = \beta_L - \beta_1$). R_d , L , b , and h represent disk radius, blade length, blade width, and blade thickness, respectively.

(1) Verification by using the first FE model

In the first FE model, the blade is simulated by a Timoshenko beam (Beam188 element), and the shroud is described by a lumped-mass point (Mass21 element). The twisted beam is established by changing the shape of the beam section. This modeling process can be realized by setting the section type of Beam188 to “Quad”. The blade modeling is completed by changing the coordinates of the four corner points of the rectangular cross section (i.e., corner points A_n , B_n , C_n , and D_n in Fig. 5(b)). In this study, $n = 61$ sections are adopted in the blade length direction (i.e., x -direction), and the distance of adjacent sections are all set to $L/(n - 1)$, as shown in Fig. 5(a). On the basis of the geometric relationships in Fig. 5(b), the y - and z -direction coordinates of Points C_n and D_n are expressed as follows:

$$\begin{cases} z_{C_n} = \frac{d}{2} \cos\beta_n + \frac{h}{2} \sin\beta_n, \\ y_{C_n} = -\frac{d}{2} \sin\beta_n + \frac{h}{2} \cos\beta_n, \\ z_{D_n} = \frac{d}{2} \cos\beta_n - \frac{h}{2} \sin\beta_n, \\ y_{D_n} = -\frac{d}{2} \sin\beta_n - \frac{h}{2} \cos\beta_n, \end{cases} \quad (13)$$

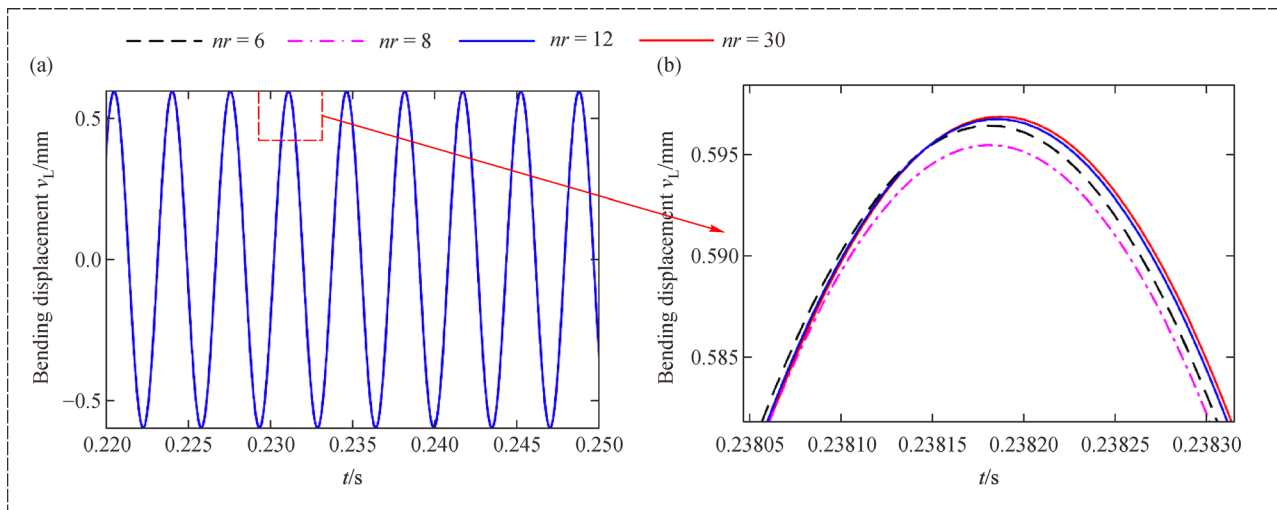


Fig. 3 Vibration responses of the bending displacement of the blade tip under $\Delta = 0.6$ mm at $\Omega = 8500$ r/min: (a) Displacement waveforms and (b) partial enlarged waveforms.

Table 2 Shrouded blade parameters

Young's modulus/GPa	Density/(kg·m ⁻³)	Poisson's ratio	Disk radius/mm	Blade length/mm	Blade width/mm
200	7800	0.3	150	150	40
Blade thickness/mm	Stagger angle/(°)	Shroud length/mm	Shroud width/mm	Shroud thickness/mm	Twist angle/(°)
7	30	40	20	7	10

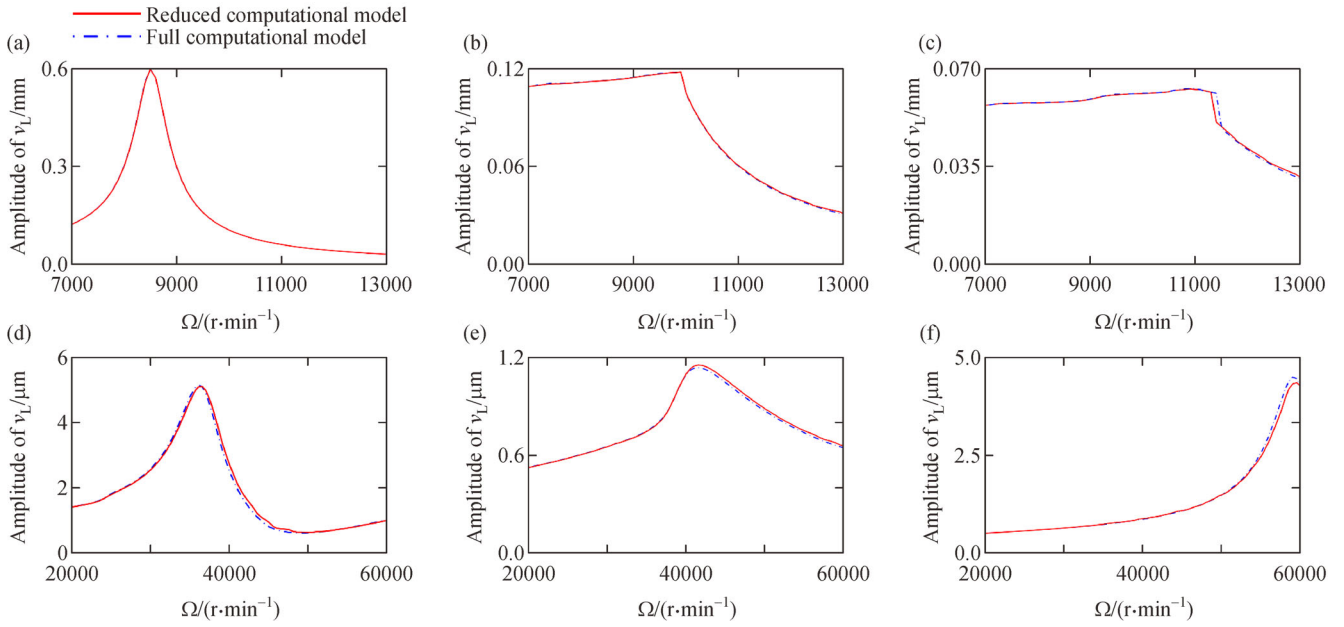


Fig. 4 Amplitude–frequency responses obtained from the reduced and full computational models: (a) $\Delta = 0.6$ mm, (b) $\Delta = 0.1$ mm, (c) $\Delta = 0.05$ mm, (d) $N_0 = 0$ N, (e) $N_0 = 10$ N, and (f) $N_0 = 50$ N.

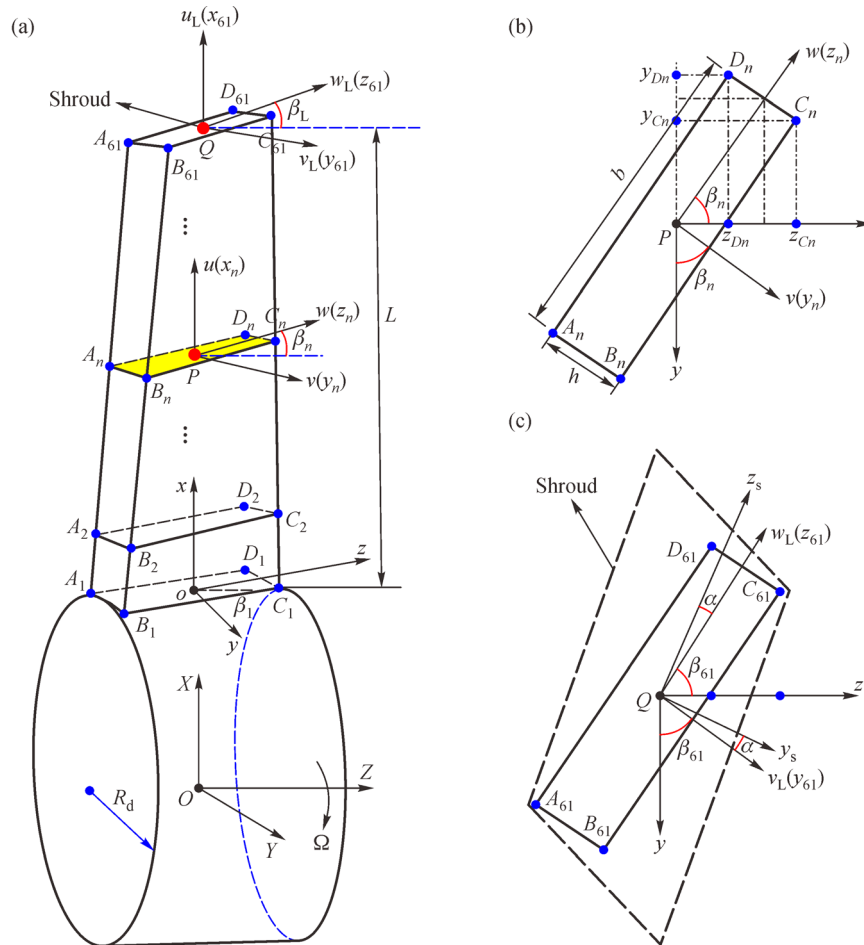


Fig. 5 Schematics of the FE models of the shrouded blade: (a) Blade model, (b) arbitrary blade section, and (c) shroud inclination angle α .

where $\beta_n = \beta_1 + (i-1)\beta'/(n-1)$ ($i=1, 2, \dots, n$, here, $n = 61$). Points A_n and C_n and points B_n and D_n are symmetric to origin P ; therefore,

$$z_{An} = -z_{Cn}, y_{An} = -y_{Cn}, z_{Bn} = -z_{Dn}, y_{Bn} = -y_{Dn}. \quad (14)$$

In the first FE model (Fig. 6), 60 Beam188 elements and 61 nodes are used to simulate the blade, and each node has 6 DOFs. One Mass21 element is adopted to simulate the shroud, and two point–point contact elements (Conta178 elements) are used to simulate impact and friction. The directions of the contact elements should be determined on the basis of the shroud inclination angle, particularly by

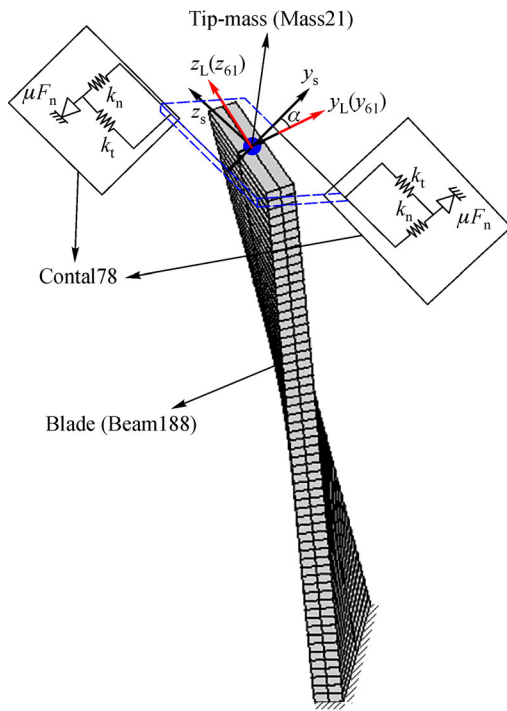


Fig. 6 Schematic of the first FE model by using ANSYS.

specifying the contact normal direction and by using real constants. The node of the blade root is fully constrained, and the rotational DOF on the X -axis for all nodes is constrained (i.e., the torsional vibration of the shrouded blade is constrained). Rayleigh damping is also adopted in the first FE model (Eq. (2)). With the aim of improving computational efficiency, the free-interface modal synthesis method is used to reduce the FE model dimension. In the reduction dimension process, the blade is selected as a substructure, the blade tip node is defined as the main node, and the truncation order is set to 24. Thus, the dimensions of the mass matrix, stiffness matrix, and damping matrix can all be set to 30×30 , which is the same as those of the proposed computational model.

The amplitude–frequency responses of blade tip point obtained from the full and reduced models under different initial gaps and normal loads, in which the other parameters are the same as above, are shown in Fig. 7. In Fig. 7, the lines and the point denote the results obtained from the reduced computational and FE models, respectively. The amplitude–frequency responses obtained from two models are in good agreement with one another under different conditions. This finding also verifies the effectiveness of the reduced computational model in impact–friction conditions.

The vibration responses obtained from the four models (reduced computational model, full computational model, reduced FE model, and full FE model) are compared to verify the correctness of the established models (Fig. 8). The selected system simulation parameters are as follows: $\Omega = 10000$ r/min, $N_0 = 0$ N, $k_t = 1 \times 10^7$ N/m, $k_n = 1 \times 10^7$ N/m, $\alpha = 15^\circ$, and $\mu = 0.3$. In Figs. 8(d) and 8(h), States 1–3 represent the separation, slip, and stick states, respectively. The vibration responses obtained from the four models are in good agreement with one another in terms of time-domain waveforms and hysteresis loops. The calculation times (100 periods, with sampling interval of $60/(256k_c\Omega)$ s) of the four models are shown in Table 3.

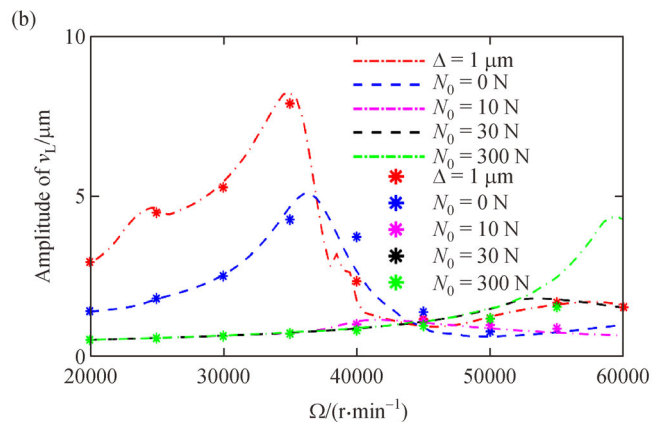
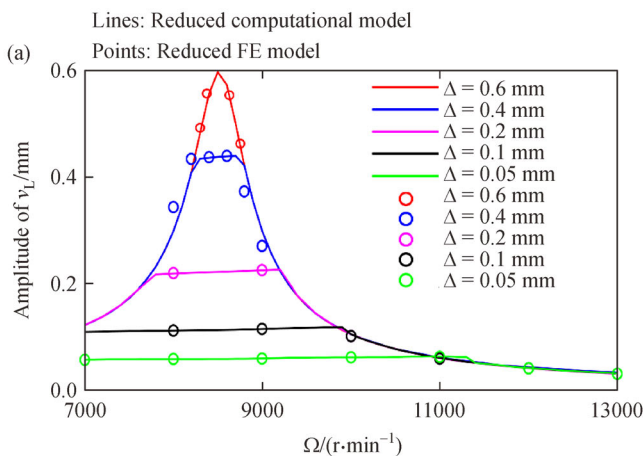


Fig. 7 Amplitude–frequency responses: (a) Different initial gaps and (b) small initial gap ($\Delta = 1 \mu\text{m}$) and different initial normal preloads.

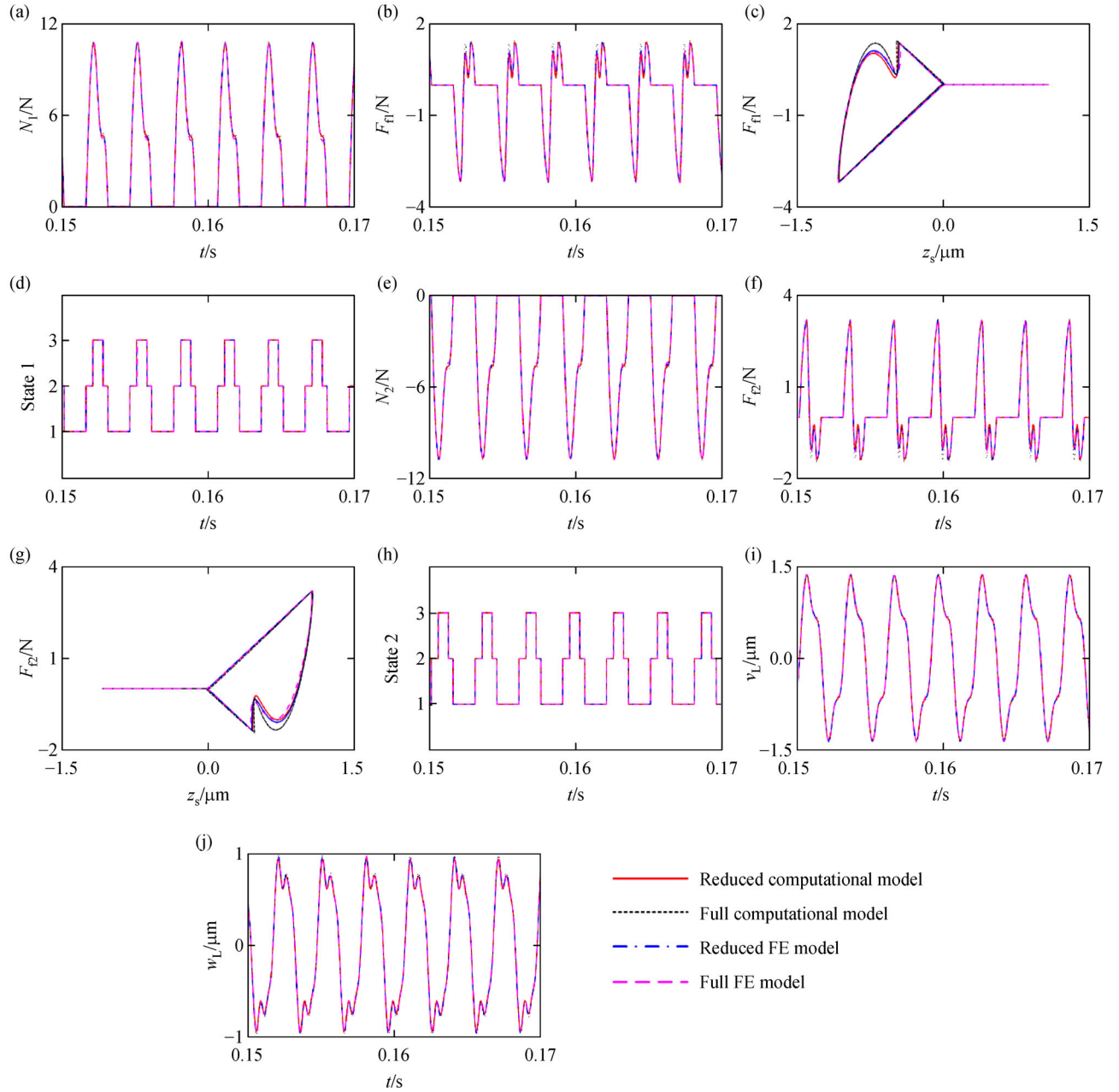


Fig. 8 Response comparisons among the four models: (a) Impact force on the left side of the shroud, (b) friction force on the left side of the shroud, (c) hysteresis loop on the left side of the shroud, (d) contact state on the left side of the shroud, (e) impact force on the right side of the shroud, (f) friction force on the right side of the shroud, (g) hysteresis loop on the right side of the shroud, (h) contact state on the right side of the shroud, (i) displacements in flexural direction, and (j) displacements in swing direction.

Table 3 Calculation times of the four models

Model	Calculation time/s
Reduced computational model	5.37
Full computational model	7.66
Reduced FE model	2328.84
Full FE model	3259.67

The efficiencies of the reduced models are nearly 30% better than the efficiencies of the full models. The proposed computational models have higher computational efficiencies than the FE models because the contact elements in the latter need several iterations to obtain the convergent results. The difference in calculation time can also be attributed to the software.

(2) Verification by using the second FE model

The second FE model with Shell181 elements is established to further evaluate the proposed computational model (Fig. 9). The blade and the shroud are discretized into 200 and 60 elements, respectively. Eleven contact elements (Conta178 elements) between the active blade shroud and each passive blade shroud are established. The second FE model also adopts Rayleigh damping (Eq. (2)). The free-interface modal synthesis method is also used to reduce the dimension of the shell FE model, in which the blade is selected as a substructure and the truncation order is set to 24. In addition, for the shroud, the middle node and the 22 nodes connected to the contact elements are defined as the main nodes.

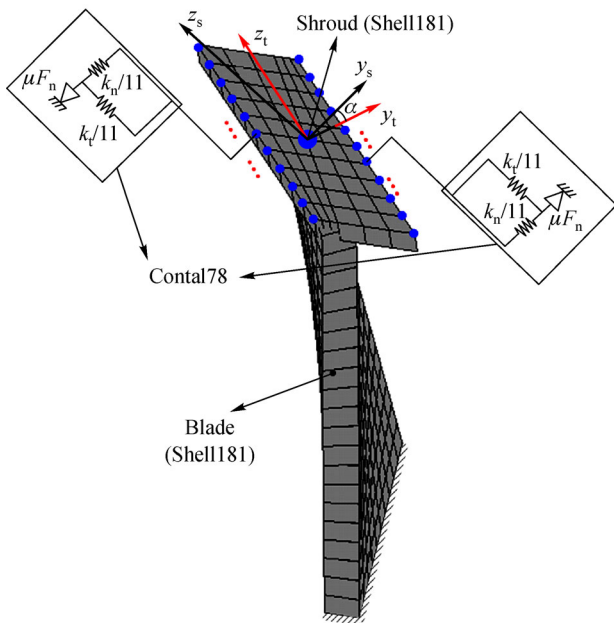


Fig. 9 Schematic of the second FE model by using ANSYS.

The comparison results obtained from the reduced computational model and the shell FE model are shown in Fig. 10. The rotational speed is $\Omega = 10000$ r/min, while

the other simulation parameters are the same as those in Fig. 8. As shown in Fig. 10, the impact and friction forces are the resultant forces at all nodes on the contact interface between the active blade and passive blade 1. The displacement of the middle node in the active blade in the flexural direction is shown in Fig. 10(c). At $\Omega = 10000$ r/min, the computation time of the reduced shell FE model (100 periods, with sampling interval of $60/(256k_c\Omega)$ s) is approximately 2605.71 s, which is slightly larger than that of the reduced beam FE model, but is remarkably higher than that of the reduced computational model proposed in this study. The comparison results show similar vibration laws, and the vibration amplitudes are larger than those of the shell FE model.

3 Vibration responses of the shrouded blade under different parameters

On the basis of the above discussion on the proposed blade model in which impact and friction have been established, the effects of initial gaps Δ and initial normal preloads N_0 , coefficient of friction μ , and contact stiffness ratio ξ on the system dynamic characteristics are analyzed. Owing to the influence of the normal motion of the shroud on the normal load, the limiting friction force is no longer a simple product of the coefficient of friction and the initial normal preload. The influences of the initial normal preload and the coefficient of friction on the vibration responses differ from one another; thus, the two effects are individually analyzed. The stagger angle and the twist angle are primarily determined by the aerodynamic design. Therefore, the influences of both angles on the vibration responses of the shrouded blade will not be elaborated in this paper. Instead, the fixed stagger angle and the twist angle are applied, i.e., the stagger angle is set to 30° , while the twist angle is set to 10° .

3.1 Case 1: Effects of initial gap and normal load

The amplitude–frequency responses of the shrouded blade under different initial gaps and normal preloads are shown

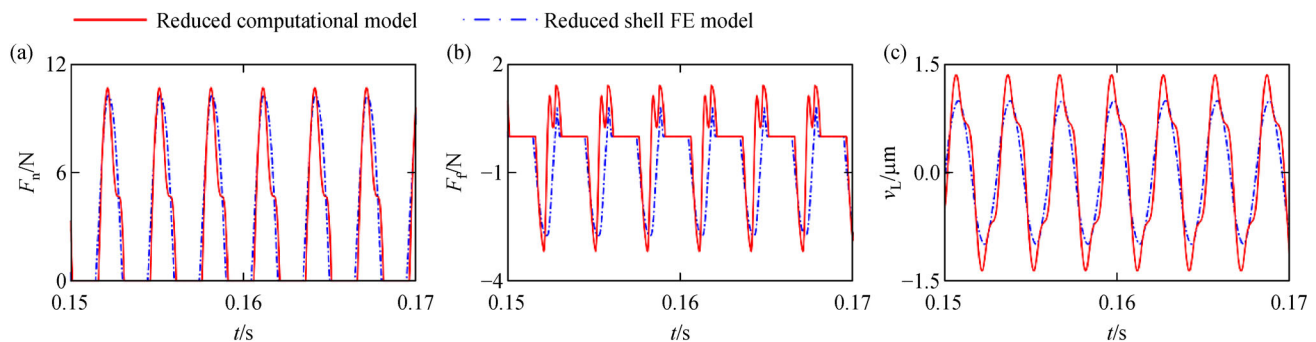


Fig. 10 Response comparison at $\Omega = 10000$ r/min: (a) Impact forces, (b) friction forces, and (c) displacements in flexural direction.

in Fig. 11. The system simulation parameters are defined as follows: $\mu = 0.3$, $\alpha = 30^\circ$, $k_t = 5 \times 10^6$ N/m, and $k_n = 1 \times 10^7$ N/m. When blade rotational speed is increased, the resonance peak of the bending displacement v_L of the blade tip becomes apparent. For example, the resonant peak appears at the rotational speed of $\Omega = 8500$ r/min under $\Delta = 0.6$ mm (Fig. 11(a)). This finding can be attributed to $2f_t$ (283.3 Hz), which is close to the first-order natural frequency of the blade (284.2 Hz in Table 1) at this rotational speed, and this phenomenon leads to the appearance of primary resonance. Two extreme cases are considered. The first case occurs when the impact and friction between the shrouded blades do not appear under the first natural frequency (the initial gap is sufficiently large), whereas the second case occurs when the initial normal preload is considerably large such that no relative slipping can occur, i.e., the damping effect disappears. Except for the two extreme cases, slip and stick contact states alternately exist between shrouds in a given vibration period, in which the initial gap decreases or the initial normal preload increases, and blade resonant speed will increase accordingly. When the initial gap decreases, the resonant peak of the blade becomes inconspicuous. This finding can be explained by the vibration of the blade that is strongly restrained by the impact force between adjacent shrouds. This phenomenon indicates the limitation of blade shrouds relative to blade vibration amplitude. In the case of initial normal preload, the existence of an optimal normal preload (a well-known phenomenon) can minimize the resonant amplitude of the blade.

3.2 Case 2: Effects of coefficient of friction

The amplitude–frequency responses of the shrouded blade with different μ are shown in Fig. 12. The resonant response characteristics of the shrouded blade with

different Δ , N_0 , and μ are shown in Fig. 13. The selected system simulation parameters are defined as follows: $\alpha = 30^\circ$, $k_t = 5 \times 10^6$ N/m, and $k_n = 1 \times 10^7$ N/m. The vibration responses at $\Omega = 25500$ r/min under $\mu = 0.1$ and $\mu = 0.5$ are shown in Figs. 14 and 15. The following dynamic phenomena can be deduced from Figs. 14 and 15:

(1) The resonant rotational speed and the resonant amplitude of the shrouded blade remain nearly unchanged under the same initial gap ($\Delta \geq 100$ μm) with the increase of μ (Figs. 12(a), 12(c), 12(e), 13(a), and 13(b)). Under a large initial gap, the contact time of adjacent shrouds becomes extremely short such that friction has negligible influence on vibration. When the initial gap is small (i.e., $\Delta = 1$ μm) or the initial normal preload N_0 is constant, the resonant rotational speed will increase with the increase of μ (Figs. 12(b), 12(d), and 12(f)).

(2) Initial normal preload decreases with the increase of μ when the contact interface nears the initial full stick state (Fig. 13(d)), i.e., the larger the coefficient of friction is, the greater the maximum friction force under the same initial normal preload will be. The shroud contact interfaces cannot easily achieve a slip. The resonant rotational speed and the amplitude become stable after the contact state is in full stick state, i.e., μ does not affect the vibration characteristics of the shrouded blade in this condition. The minimum resonant amplitude remains nearly unchanged despite the change of μ (Figs. 13(c) and 13(d)).

(3) Period-one (P1) motion and period-ten (P10) motion appear at $\mu = 0.1$ and $\mu = 0.5$, respectively (Figs. 14 and 15). P10 motion occurs because the impact period is ten times that of the aerodynamic force period (f_e is the aerodynamic frequency). The friction force has the same period as the impact force. The P10 motion leads to the fluctuation of the amplitude–frequency response in the range of [22500, 26000] r/min (Fig. 12(f)).

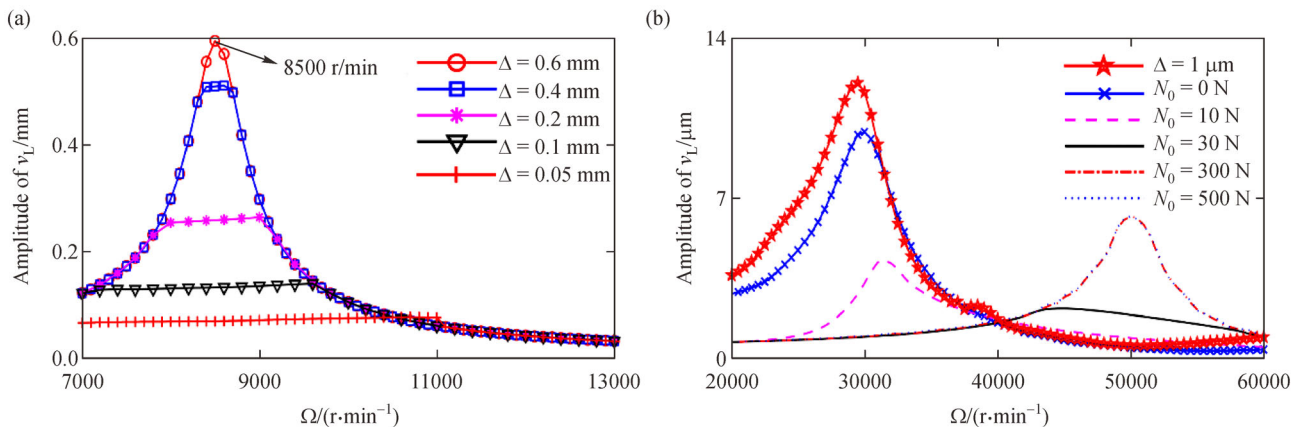


Fig. 11 Amplitude–frequency responses of shrouded blade: (a) Different initial gaps and (b) small initial gaps ($\Delta = 1$ μm) and initial normal preloads.

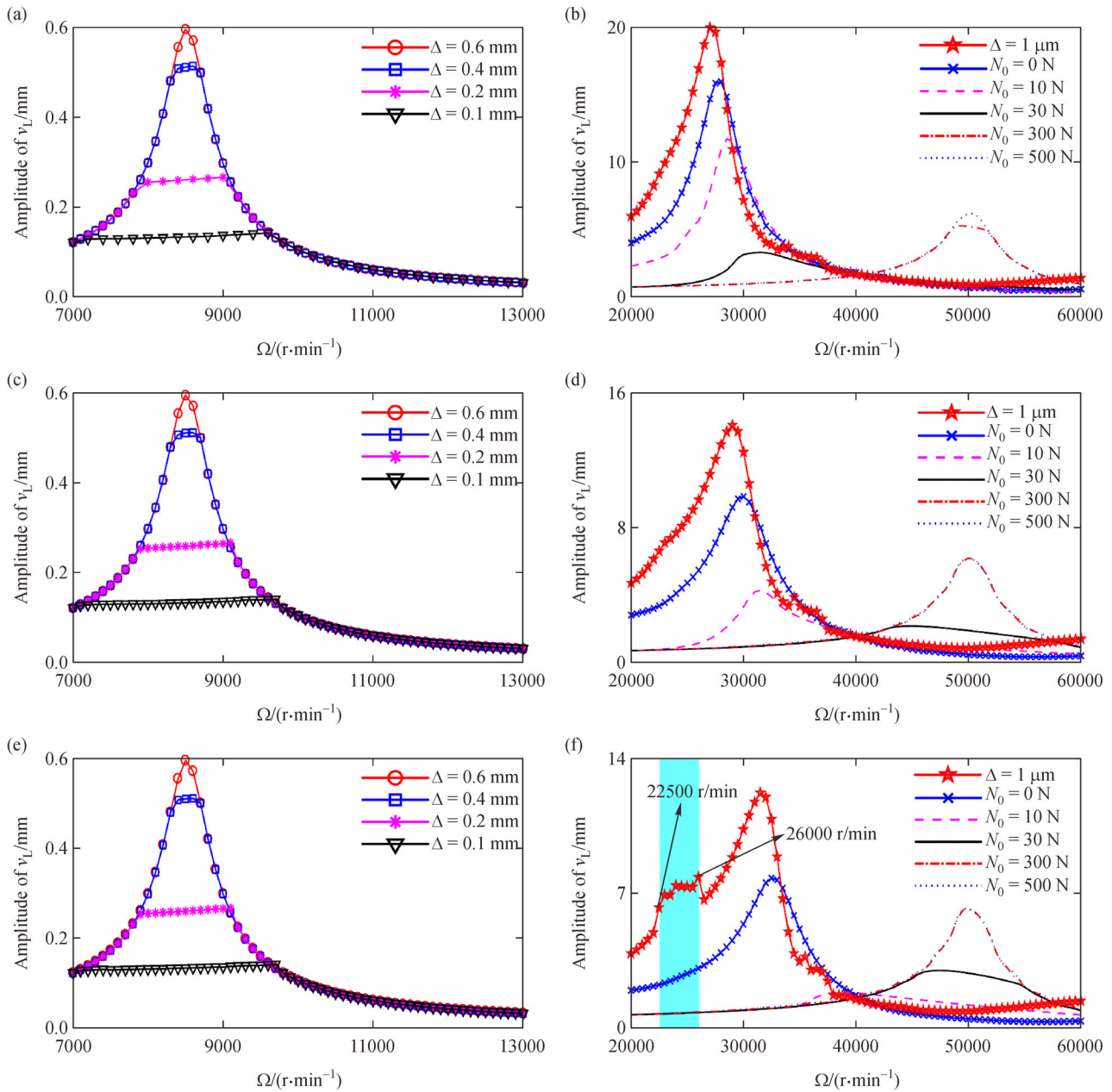


Fig. 12 Amplitude–frequency responses under different Δ , N_0 , and μ : (a) $\mu = 0.1$ under different initial gaps, (b) $\mu = 0.1$ under different initial normal preloads, (c) $\mu = 0.3$ under different initial gaps, (d) $\mu = 0.3$ under different initial normal preloads, (e) $\mu = 0.5$ under different initial gaps, and (f) $\mu = 0.5$ under different initial normal preloads.

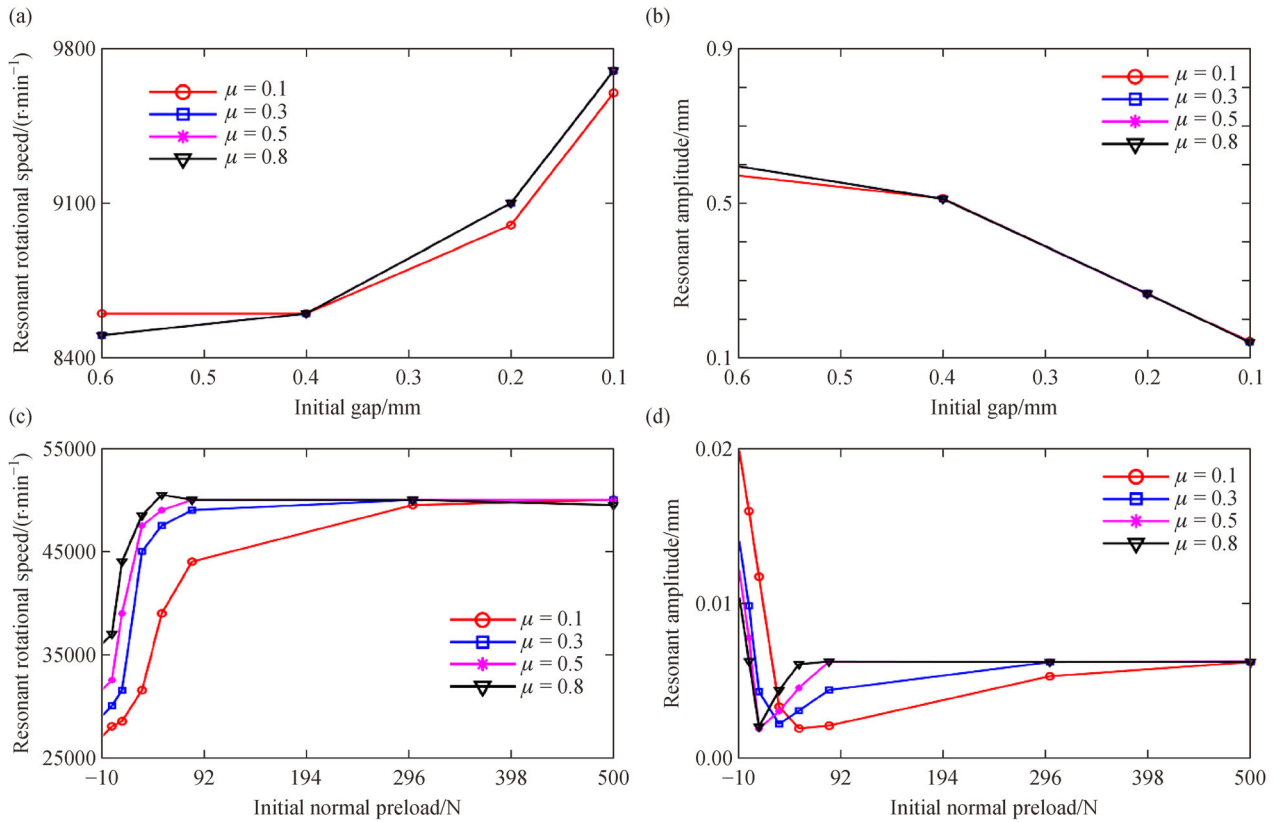


Fig. 13 Resonant response characteristics under different coefficients of friction: (a) Resonant rotational speed under different initial gaps, (b) resonant amplitude under different initial gaps, (c) resonant rotational speed under different initial normal preloads, and (d) resonant amplitude under different normal preloads.

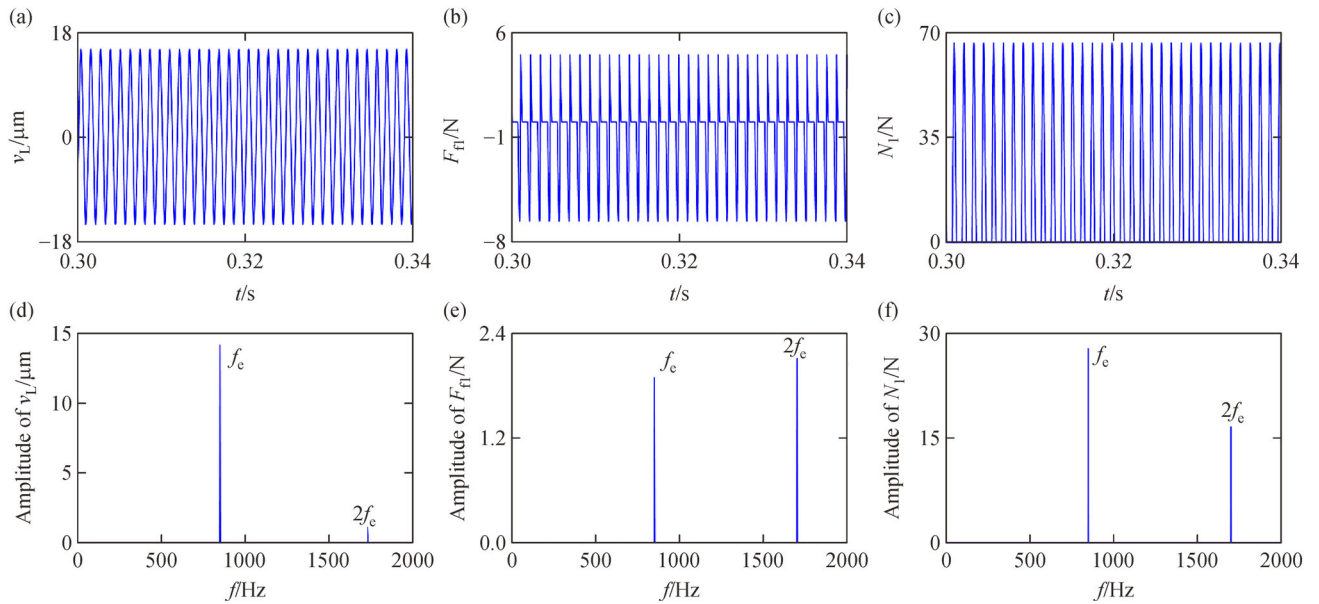


Fig. 14 Vibration responses at $\Omega = 25500 \text{ r/min}$ under $\mu = 0.1$: (a) Displacement v_L , (b) friction force F_{fr} , (c) impact force N_1 , (d) frequency spectrum of displacement, (e) frequency spectrum of friction force, and (f) frequency spectrum of impact force.

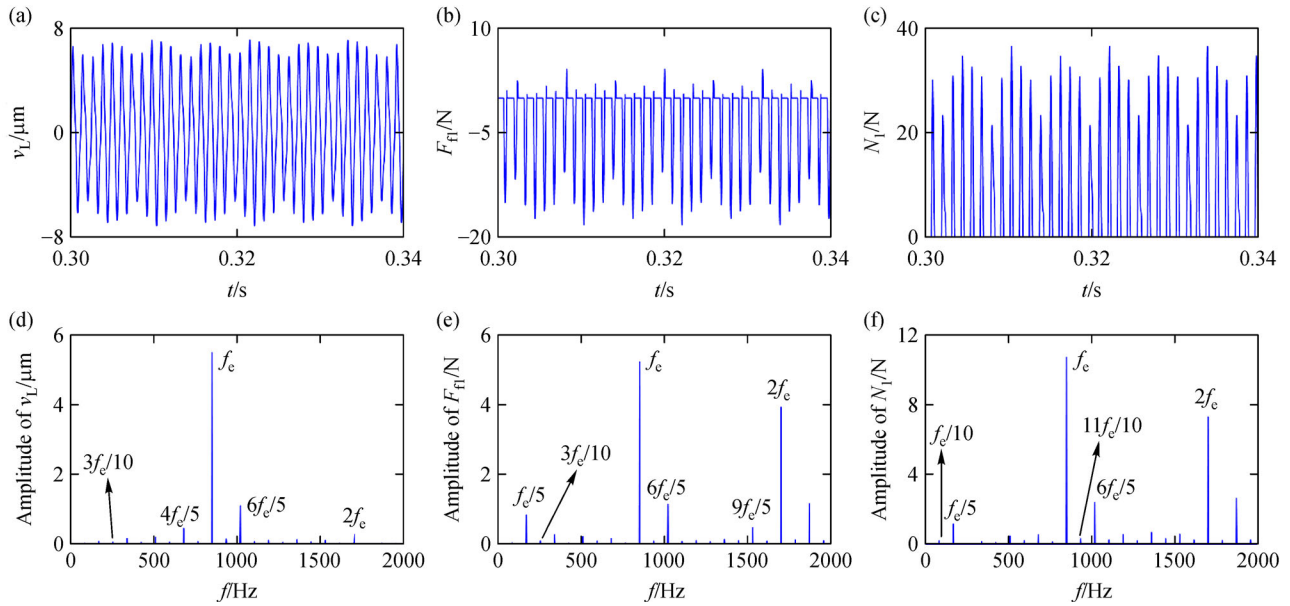


Fig. 15 Vibration responses at $\Omega = 25500$ r/min under $\mu = 0.5$: (a) Displacement v_L , (b) friction force F_{fr} , (c) impact force N_i , (d) frequency spectrum of displacement, (e) frequency spectrum of friction force, and (f) frequency spectrum of impact force.

3.3 Case 3: Effects of contact stiffness ratio

The dynamic responses of the shrouded blade under different contact stiffness ratios ($\xi = k_t/k_n$, $k_n = 1 \times 10^7$ N/m) are shown in Fig. 16. The resonant characteristics of the shrouded blade under different Δ , N_0 , and ξ are shown in Fig. 17. The selected system simulation parameters are defined as follows: $\mu = 0.3$, $\alpha = 30^\circ$, and $k_n = 1 \times 10^7$ N/m. The following dynamic phenomena can be deduced from Figs. 16 and 17:

1) The resonant rotational speed and the resonant amplitude of the shrouded blade remain nearly unchanged under the same initial gap ($\Delta \geq 100 \mu\text{m}$) with the increase of ξ (Figs. 16(a), 16(c), 16(e), 17(a), and 17(b)). This finding indicates that the tangential stiffness between shrouds has a negligible effect on the vibration responses of the shroud under large initial gaps.

2) When a small gap ($\Delta = 1 \mu\text{m}$) or an initial normal preload exists, the resonant rotational speed increases, while the resonant amplitude decreases, with the increase of ξ (Figs. 16(b), 16(d), and 16(f)). This finding indicates that the increase in contact stiffness ratio will strengthen the constrained effects between shrouds (Figs. 17(c) and 17(d)).

3) An increasing ξ will not affect the optimal initial normal preload, and this phenomenon contributes to the best damping effect. Furthermore, when the contact is under full stick, the initial normal preload will also remain unchanged (Figs. 17(c) and 17(d)). The reason behind this observation is that an increase in tangential contact stiffness does not affect the maximum friction force between shrouds.

4 Conclusions

A computational model of a twisted shrouded blade with impact and friction between adjacent shrouds is established by using Timoshenko beam theory and the macroslip friction model. The proposed computational model is verified by the FE model. Then, the effects of initial gaps Δ and initial normal preloads N_0 , coefficient of friction μ , and contact stiffness ratio ξ (the ratio of tangential contact stiffness to normal contact stiffness) on system dynamic characteristics are analyzed. The main conclusions are as follows:

1) For the investigated model in this study, under a large initial gap Δ (i.e., $\Delta \geq 100 \mu\text{m}$) between adjacent shrouds, the vibration responses of the shrouded blade are mainly affected by impact force, and the resonant peak of the shrouded blade becomes inconspicuous in this case. With the decrease of Δ , the resonant rotational speed will increase because the additional stiffness caused by adjacent shrouds increases, and the resonant amplitude will decrease due to the intensive limitation of adjacent shrouds. Furthermore, coefficient of friction μ and contact stiffness ratio ξ have almost no influence on system vibration under large Δ .

2) Friction has a remarkable influence on the vibration responses of the shrouded blade in the presence of initial normal preload or small initial gap (i.e., $\Delta = 1 \mu\text{m}$). Multiple periodic motions, such as P10 motion, can be observed under small gaps and large coefficients of friction. When slip and stick contact states between shrouds alternately exist in a given vibration period, resonant rotational speed also increases with the increase

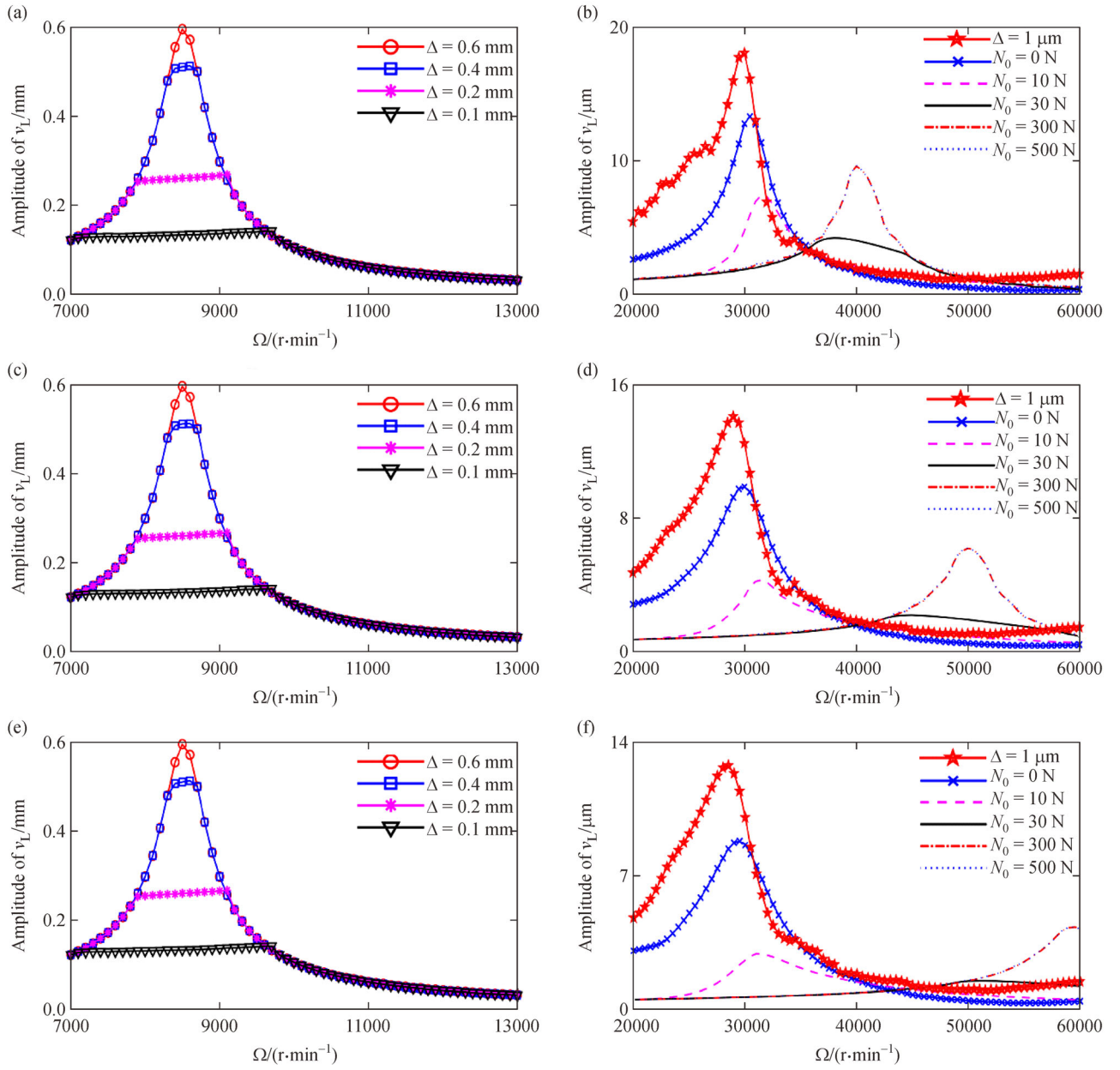


Fig. 16 Amplitude–frequency responses under different Δ , N_0 , and ξ : (a) $\xi = 0.2$ under different initial gaps, (b) $\xi = 0.2$ under different initial normal preloads, (c) $\xi = 0.5$ under different initial gaps, (d) $\xi = 0.5$ under different initial normal preloads, (e) $\xi = 1$ under different initial gaps, and (f) $\xi = 1$ under different initial normal preloads.

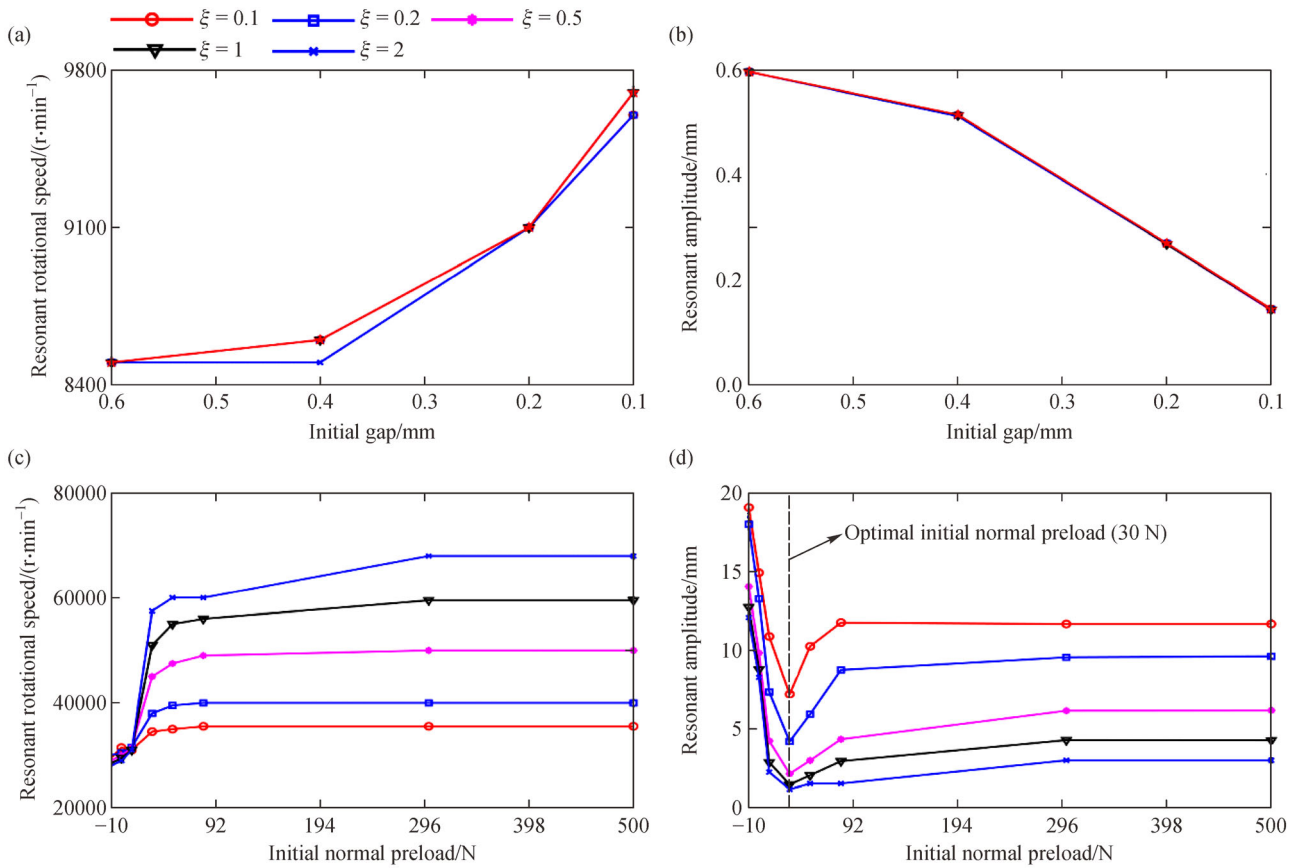


Fig. 17 Resonant response characteristics under different contact stiffness ratios: (a) Resonant rotational speed under different initial gaps, (b) resonant amplitude under different initial gaps, (c) resonant rotational speed under different initial normal preloads, and (d) resonant amplitude under different normal preloads.

of N_0 . Optimal N_0 can minimize the amplitude of the system. With the increase of coefficient of friction, the optimal N_0 tends to decrease, while the minimum resonant amplitude nearly remains unchanged. Furthermore, contact stiffness ratio ξ hardly affects the optimal N_0 , while resonant amplitude will decrease with the increase in ξ .

Spring elements are adopted to investigate the effects of adjacent passive blades, but the inertial effects of adjacent blades are ignored in this study. In future work, neighboring blades or the cyclically symmetric model will be considered.

Acknowledgements This project was supported by the National Natural Science Foundation (Grant No. 11772089), the Fundamental Research Funds for the Central Universities (Grant Nos. N170306004, N170308028, N180708009, and N180306005), the Program for the Innovative Talents of Higher Learning Institutions of Liaoning (Grant No. LR2017035), and Liaoning Revitalization Talents Program (Grant No. XLYC1807008).

Nomenclature

A Cross-sectional area of the blade
 b Blade width

D, D^*	Rayleigh damping matrices before and after dimension reduction
E	Young's modulus
F, \bar{F}	Canonical external force vectors without and with impact and friction
F^*	Canonical external force vector after dimension reduction
F_∞, F_0	Uniformly distributed aerodynamic force per unit length and aerodynamic force amplitude
F_y, F_z	Components of impact and friction force in the flexural and swing directions
F_{r1}, F_{r2}	Friction force
$f_c(x)$	Centrifugal force of the shrouded blade
f_e	Aerodynamic frequency
f_r	Rotational frequency
f_{n1}, f_{n2}	The first two-order natural frequencies of the shrouded blade
G, G^*	Coriolis force matrices before and after dimension reduction
h	Blade thickness
I_y, I_z	Area moment of inertias of y and z axes of the blade section

K, K^*	Stiffness matrices before and after stiffness reduction
K_c, K_{c_0}, K_s	Structural stiffness matrix, centrifugal stiffening matrix, and spin softening matrix
K_{acc}	Stiffness matrix caused by angular acceleration
k_t, k_n	Tangential and normal contact stiffness
L	Blade length
M, M^*	Mass matrices before and after dimension reduction
N	Number of modal truncation
nr	Dimension of matrix after dimension reduction
n	Section number of the first FE model
N_0	Initial normal preload
N_1, N_2	Impact force
N^*	Dimension reduction matrix
m_s	Shroud mass
q, q^*	Canonical coordinate vectors of the blade before and after dimension reduction
R_d	Radius of disk
v_L, w_L	Bending and swing displacements at blade tip
v_s, w_s	Tangential and normal displacements of shroud
z_{s1}	Tangential displacement of active blade shroud
z_{s2}, z_{s3}	Displacements of contact point
ρ	Density of the blade
θ	Rotational angle of the disk
β'	Twist angle of shrouded blade
β_1, β_L	Stagger angle at the root and blade tip of the blade
β_n	Angle of an arbitrary cross section between z axis and z_n axis
$\beta(x)$	Twist angle of an arbitrary Point P of the blade
Ω	Rotational speed/($r \cdot \text{min}^{-1}$)
$\phi_1(x), \phi_2(x), \phi_3(x)$	i th modal shape functions in radial, flexural/swing, and rotational angle directions
Δ	Initial gap
μ	Coefficient of friction
α	Shroud inclination angle
ξ	Contact stiffness ratio
ξ_1, ξ_2	First and second modal damping ratios
ω	Angular velocity of the blade/($\text{rad} \cdot \text{s}^{-1}$)
FE	Finite element

References

- Pennacchi P, Chatterton S, Bachschmid N, et al. A model to study the reduction of turbine blade vibration using the snubbing mechanism. *Mechanical Systems and Signal Processing*, 2011, 25(4): 1260–1275
- Allara M. A model for the characterization of friction contacts in turbine blades. *Journal of Sound and Vibration*, 2009, 320(3): 527–544
- Chu S M, Cao D Q, Sun S P, et al. Impact vibration characteristics of a shrouded blade with asymmetric gaps under wake flow excitations. *Nonlinear Dynamics*, 2013, 72(3): 539–554
- Petrov E P, Ewins D J. Effects of damping and varying contact area at blade-disk joints in forced response analysis of bladed disk assemblies. *Journal of Turbomachinery*, 2006, 128(2): 403–410
- Allara M, Zucca S, Gola M M. Effect of crowning of dovetail joints on turbine blade root damping. *Key Engineering Materials*, 2007, 347: 317–322
- Yang B D, Menq C H. Characterization of contact kinematics and application to the design of wedge dampers in turbomachinery blading: Part 1—Stick-slip contact kinematics. *Journal of Engineering for Gas Turbines and Power*, 1998, 120(2): 410–417
- Yang B D, Menq C H. Characterization of contact kinematics and application to the design of wedge dampers in turbomachinery blading: Part 2—Prediction of forced response and experimental verification. *Journal of Engineering for Gas Turbines and Power*, 1998, 120(2): 418–423
- Sanliturk K Y, Ewins D J, Stanbridge A B. Underplatform dampers for turbine blades: Theoretical modeling, analysis, and comparison with experimental data. *Journal of Engineering for Gas Turbines and Power*, 2001, 123(4): 919–929
- Petrov E P, Ewins D J. Advanced modeling of underplatform friction dampers for analysis of bladed disk vibration. *Journal of Turbomachinery*, 2007, 129(1): 143–150
- He B P, Ouyang H J, Ren X M, et al. Dynamic response of a simplified turbine blade model with under-platform dry friction dampers considering normal load variation. *Applied Sciences*, 2017, 7(3): 228
- Petrov E P, Ewins D J. Analytical formulation of friction interface elements for analysis of nonlinear multi-harmonic vibrations of bladed disks. *Journal of Turbomachinery*, 2003, 125(2): 364–371
- Cao D Q, Gong X C, Wei D, et al. Nonlinear vibration characteristics of a flexible blade with friction damping due to tip-rub. *Shock and Vibration*, 2011, 18(1–2): 105–114
- Cao D X, Liu B Y, Yao M H, et al. Free vibration analysis of a pre-twisted sandwich blade with thermal barrier coating layers. *Science China. Technological Sciences*, 2017, 60(11): 1747–1761
- Wang D, Chen Y S, Hao Z F, et al. Bifurcation analysis for vibrations of a turbine blade excited by air flows. *Science China. Technological Sciences*, 2016, 59(8): 1217–1231
- Yang X D, Wang S W, Zhang W, et al. Dynamic analysis of a rotating tapered cantilever Timoshenko beam based on the power series method. *Applied Mathematics and Mechanics*, 2017, 38(10): 1425–1438
- Guo X J, Yang X D, Wang S W. Dynamic characteristics of a rotating tapered cantilevered Timoshenko beam with preset and pre-twist angles. *International Journal of Structural Stability and Dynamics*, 2019, 19(4): 1950043
- Zeng J, Chen K K, Ma H, et al. Vibration response analysis of a cracked rotating compressor blade during run-up process. *Mechanical Systems and Signal Processing*, 2019, 118: 568–583
- Zeng J, Ma H, Yu K, et al. Coupled flapwise-chordwise-axial-torsional dynamic responses of rotating pre-twisted and inclined cantilever beams subject to the base excitation. *Applied Mathematics and Mechanics*, 2019, 40(8): 1053–1082
- Ma H, Wang D, Tai X Y, et al. Vibration response analysis of blade-

- disk dovetail structure under blade tip rubbing condition. *Journal of Vibration and Control*, 2017, 23(2): 252–271
20. Li B Q, Ma H, Yu X, et al. Nonlinear vibration and dynamic stability analysis of rotor-blade system with nonlinear supports. *Archive of Applied Mechanics*, 2019, 89(7): 1375–1402
 21. Qin Z Y, Han Q K, Chu F L. Analytical model of bolted disk – drum joints and its application to dynamic analysis of jointed rotor. *Proceedings of the Institution of Mechanical Engineers, Part C: Journal of Mechanical Engineering Science*, 2014, 228(4): 646–663
 22. Qin Z Y, Han Q K, Chu F L. Bolt loosening at rotating joint interface and its influence on rotor dynamics. *Engineering Failure Analysis*, 2016, 59: 456–466
 23. Qin Z Y, Yang Z B, Zu J, et al. Free vibration analysis of rotating cylindrical shells coupled with moderately thick annular plates. *International Journal of Mechanical Sciences*, 2018, 142–143: 127–139
 24. Qin Z Y, Pang X J, Safaei B, et al. Free vibration analysis of rotating functionally graded CNT reinforced composite cylindrical shells with arbitrary boundary conditions. *Composite Structures*, 2019, 220: 847–860
 25. Ferri A A, Heck B S. Vibration analysis of dry friction damped turbine blades using singular perturbation theory. *Journal of Vibration and Acoustics*, 1998, 120(2): 588–595
 26. Cigeroğlu C, Özgüven H N. Nonlinear vibration analysis of bladed disks with dry friction dampers. *Journal of Sound and Vibration*, 2006, 295(3–5): 1028–1043
 27. Wang J H, Shieh W L. The influence of a variable friction coefficient on the dynamic behavior of a blade with a friction damper. *Journal of Sound and Vibration*, 1991, 149(1): 137–145
 28. Wang J H, Chen W K. Investigation of the vibration of a blade with friction damper by HBM. *Journal of Engineering for Gas Turbines and Power*, 1993, 115(2): 294–299
 29. Sanliturk K Y, Imregun M, Ewins D J. Harmonic balance vibration analysis of turbine blades with friction damper. *Journal of Vibration and Acoustics*, 1997, 119(1): 96–103
 30. Al Sayed B, Chatelet E, Baguet S, et al. Dissipated energy and boundary condition effects associated to dry friction on the dynamics of vibrating structures. *Mechanism and Machine Theory*, 2011, 46(4): 479–491
 31. Laxalde D, Thouverez F, Sinou J J, et al. Qualitative analysis of forced response of blisks with friction ring dampers. *European Journal of Mechanics-A/Solids*, 2007, 26(4): 676–687
 32. Menq C H, Griffin J H, Bielak J. The influence of a variable normal load on the forced vibration of a frictionally damped structure. *Journal of Engineering for Gas Turbines and Power*, 1986, 108(2): 300–305
 33. Yang B D, Chu M L, Menq C H. Stick-slip-separation analysis and non-linear stiffness and damping characterization of friction contacts having variable normal load. *Journal of Sound and Vibration*, 1998, 210(4): 461–481
 34. Santhosh B, Narayanan S, Padmanabhan C. Nonlinear dynamics of shrouded turbine blade system with impact and friction. *Applied Mechanics and Materials*, 2015, 706: 81–92
 35. Koh K H, Griffin J H. Dynamic behavior of spherical friction dampers and its implication to damper contact stiffness. *Journal of Engineering for Gas Turbines and Power*, 2007, 129(2): 511–521
 36. Zhang D Y, Fu J W, Zhang Q C, et al. An effective numerical method for calculating nonlinear dynamics of structures with dry-friction: Application to predict the vibration response of blades with underplatform dampers. *Nonlinear Dynamics*, 2017, 88(1): 223–237
 37. Zhao W, Li L L, Zhang D. Study on vibration characteristics of damping blade with snubber and shroud based on fractal theory. *Thermal Science*, 2016, 20(suppl 3): 887–894
 38. Jiang J P, Li J W, Cai G B, et al. Effects of axial gap on aerodynamic force and response of shrouded and unshrouded blade. *Science China. Technological Sciences*, 2017, 60(4): 491–500
 39. Hudson R, Sinha A. Frictional damping of flutter: Microslip versus macroslip. *Journal of Vibration and Acoustics*, 2016, 138(6): 061010
 40. Marquina F J, Coro A, Gutiérrez A. Friction damping modeling in high stress contact areas using microslip friction model. In: *Proceedings of the ASME Turbo Expo 2008: Power for Land, Sea, and Air. Volume 5: Structures and Dynamics, Parts A and B*. Berlin: ASME, 2009, 309–318
 41. Ramaiah P V, Krishnaiah G. Modelling and design of friction damper used for the control of vibration in a gas-turbine blade—A microslip approach. *Proceedings of the Institution of Mechanical Engineers, Part C: Journal of Mechanical Engineering Science*, 2007, 221(8): 887–895
 42. Yuan R S, Zhou Q, Zhang Q, et al. Fractal theory and contact dynamics modeling vibration characteristics of damping blade. *Advances in Mathematical Physics*, 2014, 549430
 43. Giridhar R K, Ramaiah P V, Krishnaiah G, et al. Gas turbine blade damper optimization methodology. *Advances in Acoustics and Vibration*, 2012, 316761
 44. Wu J, Yuan R S, He Z W, et al. Experimental study on dry friction damping characteristics of the steam turbine blade material with nonconforming contacts. *Advances in Materials Science and Engineering*, 2015, 849253
 45. Koh K H, Griffin J H, Filippi S, et al. Characterization of turbine blade friction dampers. *Journal of Engineering for Gas Turbines and Power*, 2005, 127(4): 856–862
 46. Botto D, Gastadi C, Gola M, et al. An experimental investigation of the dynamics of a blade with two under-platform dampers. *Journal of Engineering for Gas Turbines and Power*, 2018, 140(3): 032504
 47. Banerjee J R. Development of an exact dynamic stiffness matrix for free vibration analysis of a twisted Timoshenko beam. *Journal of Sound and Vibration*, 2004, 270(1–2): 379–401
 48. Sinha S K. Combined torsional-bending-axial dynamics of a twisted rotating cantilever Timoshenko beam with contact-impact loads at the free end. *Journal of Applied Mechanics*, 2007, 74(3): 505–522
 49. Huo Y L, Wang Z M. Dynamic analysis of a rotating double-tapered cantilever Timoshenko beam. *Archive of Applied Mechanics*, 2016, 86(6): 1147–1161
 50. Xie F T, Ma H, Cui C, et al. Vibration response comparison of twisted shrouded blades using different impact models. *Journal of Sound and Vibration*, 2017, 397: 171–191
 51. Hou S N. Review of Modal Synthesis Techniques and a New Approach. Technical Report NASA-CR-110729, 1969
 52. Lu K, Yu H, Chen Y, et al. A modified nonlinear POD method for order reduction based on transient time series. *Nonlinear Dynamics*, 2015, 79(2): 1195–1206